JGR Atmospheres

RESEARCH ARTICLE
10.1029/2018JD028976

Key Points:
- A novel scheme for recovering the cloudy sky LST was proposed by accounting for the solar-cloud-satellite geometry effect
- The LSTs of shadowed and illuminated pixels covered by the clouds in the image can be well estimated for both MODIS and Landsat-8 data
- The method is not data specific and has a reasonable accuracy; it provides some new ideas to the surface energy balance community

Supporting Information:
- Supporting Information S1

Correspondence to:
T. Wang,
wangtx@radi.ac.cn

Citation:
Wang, T., Shi, J., Ma, Y., Husi, L., Comyn-Platt, E., Ji, D., et al. (2019). Recovering land surface temperature under cloudy skies considering the solar-cloud-satellite geometry: Application to MODIS and Landsat-8 data. *Journal of Geophysical Research: Atmospheres*, *124*, 3401–3416. https://doi.org/10.1029/2018JD028976

Received 10 MAY 2018
Accepted 26 SEP 2018
Accepted article online 12 MAR 2019
Published online 25 MAR 2019

Author Contributions:
Conceptualization: Tianxing Wang, Jiancheng Shi, Letu Husi
Formal analysis: Tianxing Wang, Jiancheng Shi, Ya Ma, Letu Husi, Tianjie Zhao, Chuan Xiong
Funding acquisition: Tianxing Wang
Investigation: Tianxing Wang, Edward Comyn-Platt
Methodology: Tianxing Wang, Ya Ma, Letu Husi
Project administration: Tianxing Wang
Resources: Tianxing Wang
Supervision: Jiancheng Shi, Letu Husi
Validation: Tianxing Wang, Ya Ma, Dabin Ji
Visualization: Edward Comyn-Platt
(continued)

Recovering Land Surface Temperature Under Cloudy Skies Considering the Solar-Cloud-Satellite Geometry: Application to MODIS and Landsat-8 Data

Tianxing Wang[1], Jiancheng Shi[1], Ya Ma[2], Letu Husi[1], Edward Comyn-Platt[3], Dabin Ji[1], Tianjie Zhao[1], and Chuan Xiong[1]

[1]State Key Laboratory of Remote Sensing Science, Jointly Sponsored by Institute of Remote Sensing and Digital Earth of Chinese Academy of Sciences and Beijing Normal University, Beijing, China, [2]Chinese Academy for Environmental Planning, Beijing, China, [3]Centre for Ecology and Hydrology, Wallingford, UK

Abstract Clouds play a significant role in the derivation of land surface temperature (LST) from optical remote sensing. The estimation of LST under cloudy sky conditions has been a great challenge for the community for a long time. In this study, a scheme for recovering the LST under cloudy skies is proposed by accounting for the solar-cloud-satellite geometry effect, through which the LSTs of shadowed and illuminated pixels covered by clouds in the image are estimated. The validation shows that the new scheme can work well and has reasonable LST accuracy with a root mean square error < 4.9 K and bias < 3.5 K. The application of the new method to the Moderate Resolution Imaging Spectroradiometer (MODIS) and Landsat-8 data reveals that the LSTs under cloud layers can be reasonably recovered and that the fraction of valid LSTs in an image can be correspondingly improved. The method is not data specific; instead, it can be used in any optical remote sensing images as long as the proper input variables are provided. As an alternative approach to derive cloudy sky LSTs based only on optical remote sensing data, it gives some new ideas to the remote sensing community, especially in the fields of surface energy balance.

1. Introduction

Land surface temperature (LST) is an important parameter for studying the surface energy budget and water cycle of the Earth system (Brunsell & Gillies, 2003; Duan et al., 2017; Kustas & Anderson, 2009; Li et al., 2013; Wan & Dozier, 1996). It is an important variable in many land applications, such as evapotranspiration (Hu & Jia, 2015; Kalma et al., 2008; Tang et al., 2017), longwave radiation budget (Wang et al., 2009; Yan et al., 2016; Wang et al., 2012; Jiao et al., 2015; Yan et al., 2016), urban heat island (Ma et al., 2010; Weng, 2009), snow melting (Chen et al., 2017), vegetation monitoring (Julien & Sobrino, 2009), drought monitoring (Wan et al., 2004), and fire detection (Giglio et al., 2003). Moreover, LST is an important forcing or intermediate data for many models, such as hydrological (Xue et al., 2013), meteorological (Baehr et al., 2015), and ecological (Pielke et al., 1998) models.

Compared with the traditional ground-based measurements, remote sensing provides an unprecedented advantage in mapping LST on the regional and even global scales with various spatial resolutions. Since the 1970s, great progress has been made in deriving LST from space, and a number of methods have been proposed to derive LST from various satellite data. Typically, these approaches can be roughly grouped into three types: (1) single-channel methods (Sobrino et al., 2004; Jiménez-Muñoz and Sobrino (2003) and Jiménez-Munoz et al. (2009); Qin et al. (2001); Jiménez-Muñoz et al., 2014), (2) split-window or multiband methods (Becker & Li, 1990; Du et al., 2015; Mao et al., 2005; Mao et al., 2008; Qian et al., 2015; Sobrino et al., 1994, 1996; Sobrino et al., 2004; Tang et al., 2008; Wan & Dozier, 1996), and (3) temperature and emissivity separation methods (Gillespie et al., 1998; Hulley & Hook, 2011; Ma et al., 2002, 2000; Paul et al., 2012; Wan & Li, 1997). However, all of the mentioned methods only work under clear skies, and none of the currently available satellite-based LST products are spatially continuous due to the presence of clouds, restricting the application of LST. Specifically, a recent study reported that the annual average of cloud fraction at a global scale can exceed 70% (Mercury et al., 2012). To weaken the influence of clouds, many cloud detection and removal approaches have been suggested (Eckardt et al., 2013;

10.1029/2018JD028976

Writing - original draft: Tianxing Wang
Writing – review & editing: Tianxing Wang, Ya Ma, Dabin Ji, Tianjie Zhao, Chuan Xiong

Hagolle et al., 2010; Li et al., 2005; Lv et al., 2016; Lyapustin et al., 2008; Paudel & Andersen, 2011; Zhu & Woodcock, 2014) for various applications. However, almost all of them were designed only for visible and infrared bands. Furthermore, a basic assumption of most cloud-remove methods is that the surface property remains unchanged over a short time (e.g., a few days; Hagolle et al., 2010; Lyapustin et al., 2008; Zhu & Woodcock, 2014), which is not true for energy-related LST or longwave radiation because they change quickly in time and space. Thus, recovering the LST of pixels contaminated by clouds is not feasible by using traditional cloud removal approaches.

Although cloud is a significant obstacle for deriving surface LST, recovering the LST under cloudy skies is not impossible. In some cases, the pixels covered by clouds in the image are visible to the sun but invisible to the sensor because of the fact that both solar and satellite have certain illumination or observing angles (Wang et al., 2017). In general, the cloudy pixels shown on a remote sensing image are only a projection of the corresponding cloud at observing direction, but not of the cloud orthographic projection on the ground. The orthographic location and the projection of the cloud will have a large deviation if the observing and the solar illumination angles are relatively large. This geometry of solar-cloud satellite makes it possible to recover the LSTs for cloudy pixels in the image. As illustrated in Figure 1, region A (i.e., B + C) is the cloud projection on the image along the observing direction of the sensor (i.e., the cloud pixels shown on the image for which the LST algorithms are not applicable), and regions C and D are the cloud shadows on the image. According to the applicability of the current LST algorithms, only the LSTs of pixels in region D can be theoretically estimated. A more detailed description of the effect of the solar-cloud-satellite geometry (SCSG) on surface energy can be found in Wang et al. (2017).

As shown in Figure 1, area B can be illuminated by the sun although it is covered by clouds in the image. Therefore, it is possible that the LSTs of such pixels can be approximated using the LST of the around clear-sky pixels through proper processing. In a similar way, the LST of area C can also be estimated from the LST of nearby cloud-shadow pixels. This is our motivation in this work.

The purpose of this paper is twofold: (1) to identify the scopes of shadow (region C in Figure 1) and the illuminated (region B in Figure 1) portions of the cloud pixels on the image based on the satellite observing angles, cloud top height, and solar angles and (2) to recover the LST of regions B and C by using the temperatures of spatiotemporally nearby clear-sky and shadow pixels, respectively. The remainder of this paper is organized as follows. Section 2 describes the data sets used in this study. Section 3 presents an approach to determine the position and scopes of shadow and illuminated regions for cloudy pixels for both Moderate Resolution Imaging Spectroradiometer (MODIS) and Landsat-8 measurements. Then, the strategy to recover the LST under a cloudy region is provided. The results and discussion are provided in section 4. Finally, the conclusion is given in sections 5.

2. Data Sets

MODIS, which is onboard the Terra and Aqua satellites, is one of the most advanced instruments currently available for global land and atmosphere monitoring as evidenced by its relatively high spectral and spatial resolutions (Justice et al., 2002; Masuoka et al., 1998). More importantly, various MODIS cloud and land products are readily accessible to the scientific community. The MODIS products used in this study are given in Table.1. Both MOD11_L2 and MOD11A2 products were used to discriminate the clear-sky LST and recover the LSTs under the cloud layer. The emissivity in MOD11_L2 and MOD11B1 were used to calculate the broadband emissivity (Cheng et al., 2013) to convert site measurements of longwave radiation to LST for validation. The illumination and observing geometry in MOD03 and the cloud top height embedded in MOD06 were used to determine the position and the scope of the shadow part (region C in Figure 1) and the illuminated part (region B in Figure 1) of the cloud projection on the image.

In addition to the MODIS products, a set of Landsat-8 images was selected for the case test (Table.1). The visible and near-infrared bands of Landsat-8 were used to identify the cloud and shadow pixels and then to estimate the cloud height. The two thermal bands were employed to derive the LST under clear-sky conditions.

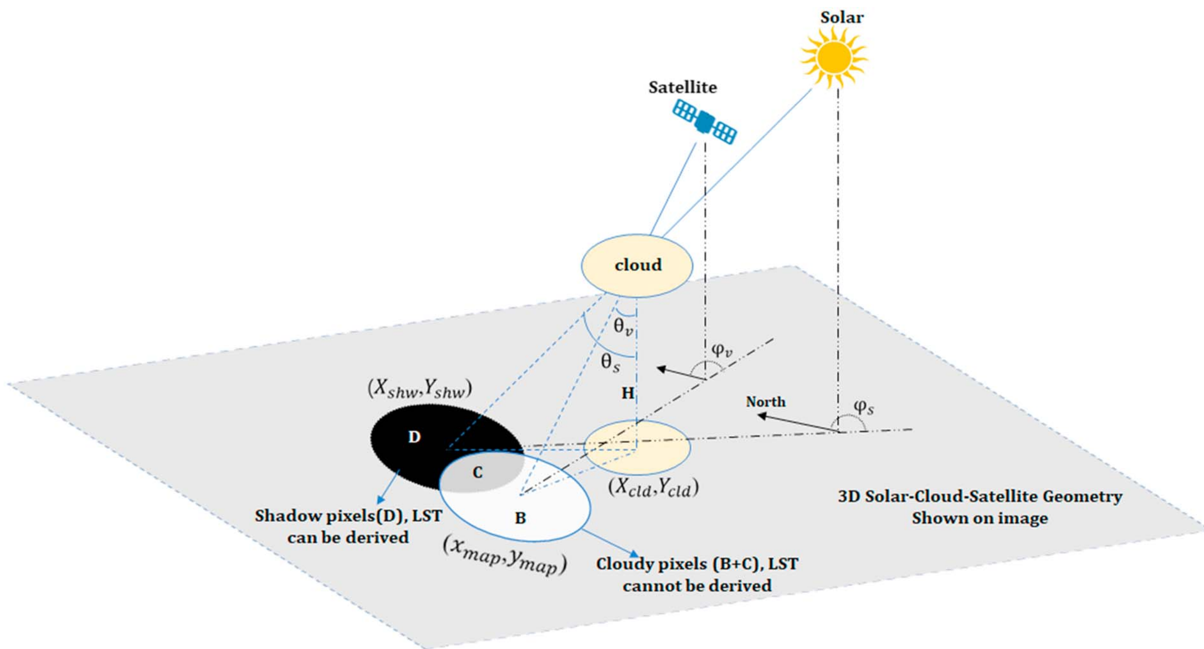

Figure 1. A 3-D schematic diagram of the solar-cloud-satellite geometry effect on the land surface temperature (LST; or surface longwave flux; pixels in regions B and C are shown as the cloud in the image; region D indicates the shadow pixels; (X_{cld}, Y_{cld}) is the cloud orthographic projection on the surface; (X_{shw}, Y_{shw}) is the orthographic position of the cloud shadow on the surface; (x_{map}, y_{map}) is the cloud position in the remote sensing image; H is cloud top height above the surface. θ_v and φ_v are the satellite observing zenith and azimuth angles, respectively, and θ_s and φ_s are the solar zenith and azimuth angles, respectively.)

3. Methods

3.1. Identification of the Scope of the Cloud and Its Shadow Due to the SCSG Effect

As illustrated in Figure 1, the cloudy pixels shown on the image consists of two parts, namely, the cloud shadow (region C) and the illuminated surface (region B). The position and the scope of these two parts should be predetermined before recovering their LSTs. According to the principle of triangular geometry, the required variables to deduce the positions of such parts are cloud top height, zenith and azimuth angles of both the solar and the observation, and the cloud projection (i.e., cloud pixels) shown on the image. In this study, for MODIS data, the required solar and satellite observing angles were extracted from the MOD03 product, and the cloud top height was obtained from the MOD06 product. For Landsat-8 images, the required angle information was extracted from the corresponding metadata file. First, the orthographic positions of the clouds were determined using equation (1), and then the positions of the associated cloud shadows were estimated using equation (2) (Wang et al., 2017).

$$X_{cld} = x_{map} + H\tan\theta_v \sin\varphi_v, \quad Y_{cld} = y_{map} + H\tan\theta_v \cos\varphi_v, \tag{1}$$

$$X_{shw} = X_{cld} - H\tan\theta_s \sin\varphi_s, \quad Y_{shw} = Y_{cld} - H\tan\theta_s \cos\varphi_s, \tag{2}$$

where (X_{cld}, Y_{cld}) is the cloud orthographic projection on the surface; (X_{shw}, Y_{shw}) is the orthographic position of the cloud shadow on the surface; (x_{map}, y_{map}) is the cloud position in the remote sensing image and is probably a pseudo position (projected along the satellite observing direction); and H is the cloud top height above the surface, which is determined by subtracting the surface altitude (in the MOD03 product) from the cloud top height (in the MOD06 product) for MODIS. The cloud top height of the Landsat-8 images was estimated by using the difference of

Table 1
MODIS Products and Landsat-8 Data Used in This Study

Product name	Resolution	Parameters
MOD11_L2	1 km	LST Emis_31 Emis_32
MOD11A2	1 km	8-day LST_Day_1 km
MOD11B1	6 km	Emis_29
MOD021KM	1 km	Radiance of bands 1–7
MCD12Q1	0 .5 km	Land Cover Type 1
MOD06	1 km	Cloud top height
MOD03	1 km	View zenith/azimuth angle Solar zenith/azimuth angle Elevation
Landsat-8	30/100 m	Bands 1–7 Bands 10 and 11

Note. LST = land surface temperature; MODIS = Moderate Resolution Imaging Spectroradiometer.

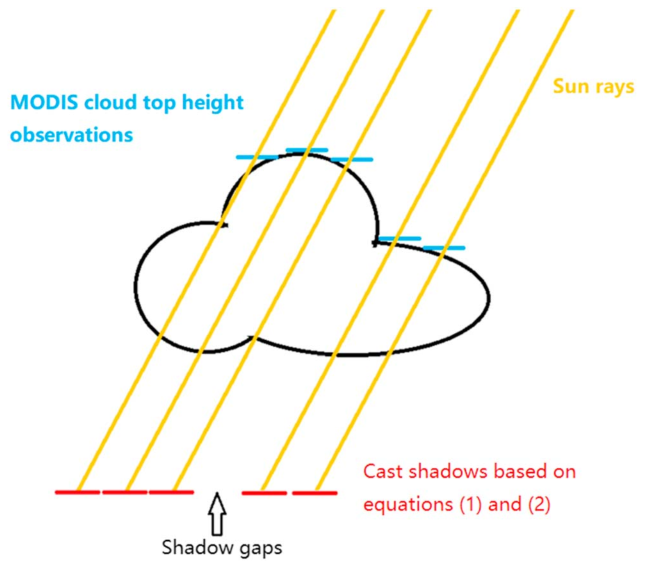

Figure 2. A schematic diagram to show the shadow gaps resulted from the large difference in cloud top heights of nearby cloud pixels.

cloud top brightness temperature and LST, which was followed by an iterative optimization between the projected shadows and the actual image shadows (section 3.2). θ_v and φ_v are the satellite observing zenith and azimuth angles, and $\theta_s$and φ_s are the solar zenith and azimuth angles, respectively. Note that in equations (1) and (2), the azimuth angle is in the range of [−180°, 180°], the true north is at 0° azimuth, east has an azimuth of 90°, and west has an azimuth of −90°. A 3-D demonstration of these variables is also indicated in Figure 1.

In general, the remotely sensed cloud top height is derived pixel by pixel; that is, a big cloud with continues heights is divided into many discrete heights, and each cloud (a pixel) is deemed as a single 2-D layer. In this case, if the height difference between two nearby cloud pixels is large, these clouds may result in shadow gaps (see Figure 2) on the surface following equations (1) and (2) when the sunlight illuminate the top of the clouds at certain zenith angles. This is unreasonable for a cloud that is inherently continuous. To avoid the gaps, the MOD06 cloud top height was smoothed using a mean filter with a 7 × 7 window. In addition, many pseudo cloud heights were found in MODIS cloud product (Figure 3). It can be seen from Figure 3b that some areas are recognized as cloudy, although they are visually completely clear. Furthermore, many unreasonable hard boundaries (yellow arrows in Figure 3b) between cloudy and clear regions are detected. In this study, a threshold (1,600 m) was used to screen out these pixels with unreasonable cloud top heights.

3.2. Optimal Estimation of Cloud Height for Landsat-8 Data

Unlike MODIS, Landsat-8 does not have a cloud height product, which is indispensable for determining the scope of a cloud and its shadow. For this point, after many tests, two thresholds were selected to simply identify the cloud and shadow based on the radiance of bands 10 and 1, respectively. Then, the clear-sky LSTs were derived by using a typical split window method (Du et al., 2015; Ren et al., 2015). The initial height for each cloud pixel was approximated by using equation (3) based on the lapse rate (Cosgrove et al., 2003):

$$Cld\_Hi = \frac{LST - T^i_{cld}}{6.5}, \tag{3}$$

where *Cld_Hi* is the cloud top height for pixel *i*; LST is the average temperature of the clear-sky pixels (Du et al., 2015; Ren et al., 2015) around the cloud in the Landsat-8 image; and T^i_{cld} is the cloud top brightness temperature for pixel *i*, which was determined by using the radiance of band 10 of Landsat-8 (equation (4)).

$$BT = \frac{K2}{\ln\left(\frac{K1}{Rad}\right) + 1}, \tag{4}$$

where *BT* is the TOA brightness temperature; *Rad* is the radiance of the thermal band (i.e., band 10); and *K*1 and *K*2 are the constants with values of 774.89 and 1,321.08 for band 10, respectively. Considering that our study area is not very large, all cloudy pixels were considered as a big cloud and assigned an average initial altitude.

As only a simple assumption of the cloud top temperature and lapse rate is used in equation (3), the derived cloud altitude generally with high uncertainties cannot be directly used to predict the cloud projection, and a refinement should be further conducted to estimate the proper cloud height. To this end, an iterative optimization scheme was employed. First, taking the initial cloud altitude derived from equation (3) as an initial value, equations (1) and (2) were then iteratively applied to predict a new shadow image when a new cloud height was assigned. During the iteration, the correlation coefficient between the predicted new shadow image (for each iteration) and the abovementioned shadow image generated in section 3.2 (based on radiances of bands 10 and 1) served as a cost function. After many iterations, the cloud height was finally determined when the cost function (correlation coefficient) reached its maximum. Given the cloud top height, the scopes of the regions of B, C, and D (Figure 1) can be determined straightforwardly for the

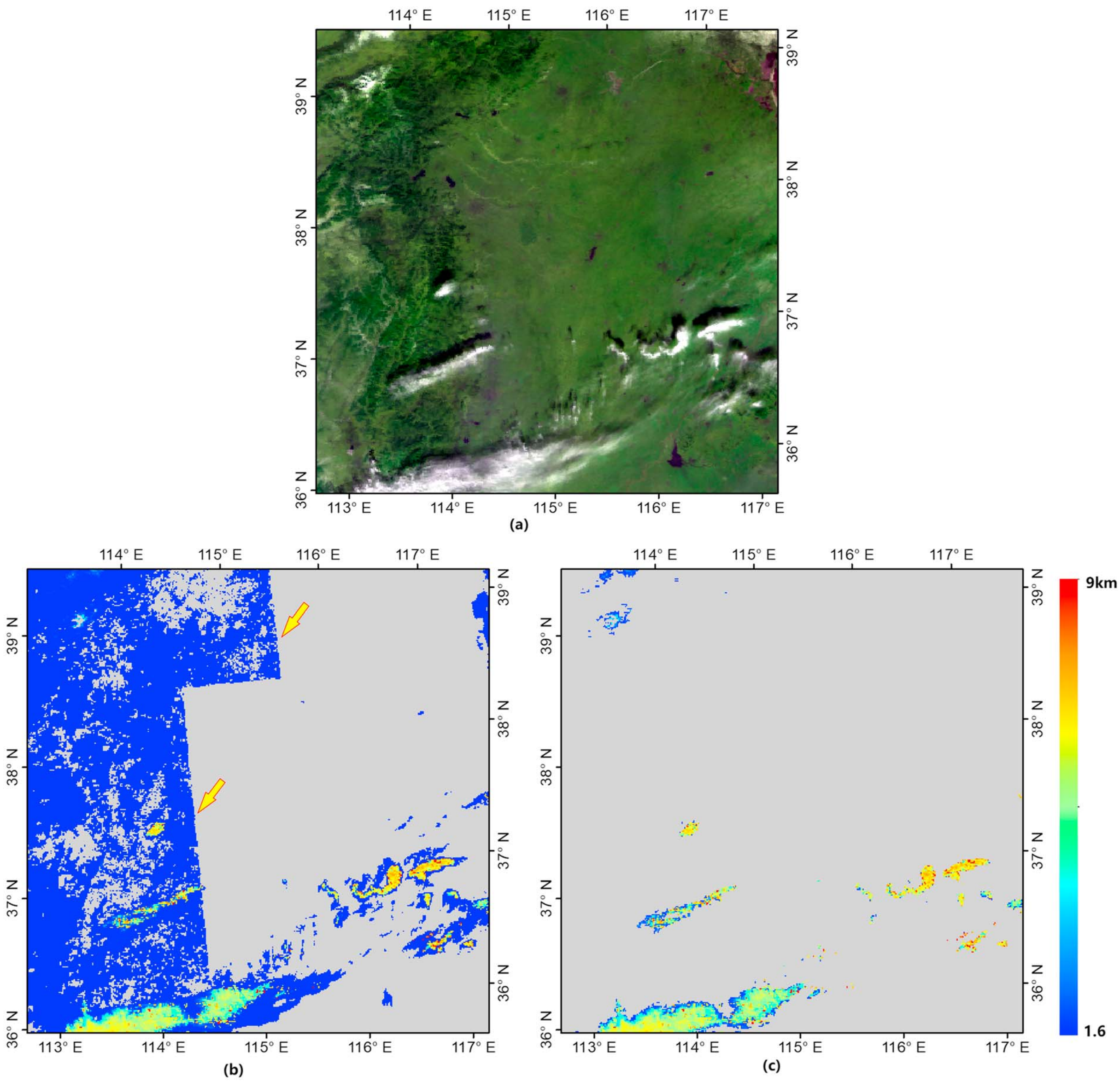

Figure 3. Cloud top height extracted from MOD06 product on 22 January 2010. (a) Moderate Resolution Imaging Spectroradiometer composite (bands 1, 2, and 3 for Red, Green and Blue (RGB) bands, respectively); (b) MOD06 product; (c) screened cloud height based on a threshold of 1,600 m.

Landsat-8 imagery. The comparison between the cloud height derived using equation (3) and that based on the above optimization method is analyzed in section 4.1.

3.3. Recovering the LST for Cloudy Pixels

3.3.1. Recovering the LST for Illuminated Areas (Region B)

Because the illuminated areas covered by the cloudy pixels (region B) on the image are not affected by the cloud, the corresponding LSTs should be similar to those under clear-sky conditions. In this study, the 8-day MODIS LST product was selected as a clear-sky reference to approximate the LSTs of the pixels in region B. Note that here we only approximate the spatial pattern of LSTs in region B but do not directly fill the corresponding pixels using the specific values of 8-day LSTs because we can never think the atmospheric and land surface conditions of the 8-day LST product are exactly the same as the image in which the cloudy pixels' LSTs need to be recovered. In this study, the recovery of LST was performed in four steps: (1) to find a clear-sky reference region (hereinafter referred to as *Clear_Region*), which is geographically collocated in both the image being studied (hereinafter referred to as *IMG-target*) and the corresponding 8-day LST

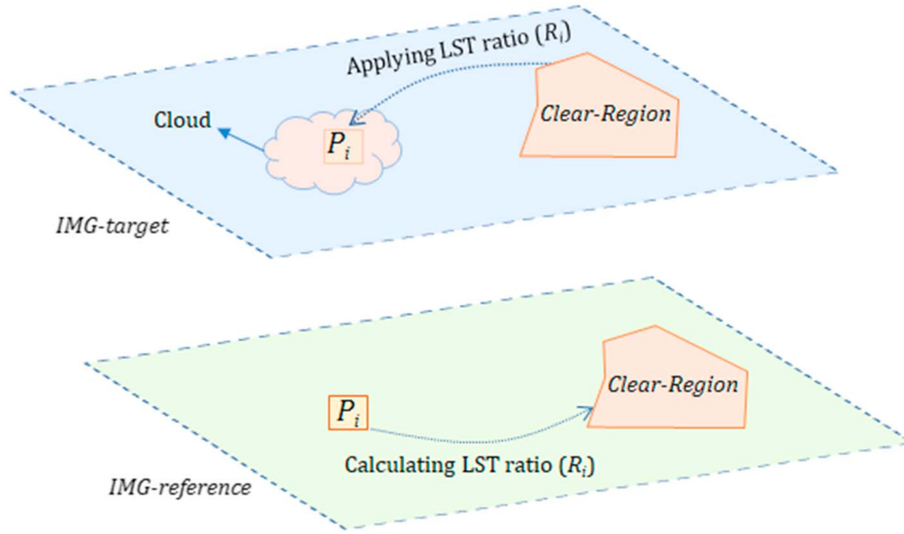

Figure 4. A sketch map to show the clear-sky reference region (*Clear-Region*) as well as the calculation and application of the LST radio during the LST recovery (*IMG-target*, the image being studied; *IMG-reference*, the clear-sky LST reference image; P_i, a typical pixel of the image; ratio (R_i), equal to the LST of the pixel (P_i), which is divided by the average LST of the *Clear_Region* pixels in the *IMG-reference*). LST = land surface temperature.

image (hereinafter referred to as *IMG-reference*)—a sketch map is shown in Figure 4 to help the readers to better understand the method. To make our scheme simple and easy to use, all the clear-sky pixels collocated in both scenes (*IMG-target* and *IMG-reference*) were chosen as the reference region (*Clear_Region*) in this paper—(2) to calculate the ratio (R_i) of the LST of each illuminated pixel (P_i) to the average LST of the *Clear_Region* pixels in the *IMG-reference*—this step is performed to build a relationship between the LST of a certain illuminated pixel and the average LST of all the clear-sky pixels within the reference region (*Clear_Region*)—(3) the LST ratio (R_i) calculated above is then assigned to the collocated pixel (P_i; region B in Figure 1) in the *IMG-target*—it should be noted that, here, the assumption behind the method is that the LST ratio (R_i) estimated from the *IMG-reference* is supposed to be consistent with that in the *IMG-target* for a certain collocated pixel within the region of B. To verify the above assumption, a comparison between the LST ratios of *IMG-target* and *IMG-reference* was conducted (Figure 5) based on more than 50 MODIS scenes, which cover most of the world's land and span from spring to winter in time. Figure 5 proves that our above assumption is believable —and (4) to recover the LST of each pixel (P_i) in *IMG-target* by multiplying the corresponding R_i and the averaged LST of the pixels within the *Clear_Region* in the *IMG-target*. A flowchart for recovering the LSTs of the illuminated pixels is shown in Figure 6.

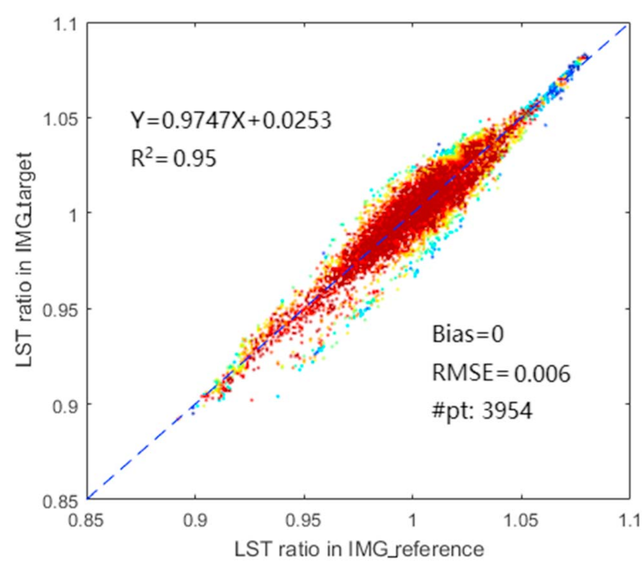

Figure 5. LST ratio comparison between the spatiotemporally collocated *IMG-target* and *IMG-reference*. LST = land surface temperature; RMSE = root mean square error.

As for the Landsat-8 data, the reference clear-sky LST image (i.e., *IMG-reference*) should be obtained from a geographically collocated Landsat-8 or comparable image acquired closest to the time of the image being studied.

3.3.2. Recovering the LST for Shadow Areas (Region C)

Unlike the illuminated region in section 3.3.1, finding a reference image (i.e., *IMG_reference*) for the shadow pixels is difficult. In this case, we assumed that the LSTs of the shadow pixels (region C), which are covered by clouds in the image, should be very similar to the LSTs of the nearby shadow pixels (region D in Figure 1). In this study, the LST of a pixel (denoted by Shw_P_i) in region C was approximated by using the average LST of all the shadowed pixels (belong to region D) within a 5 × 5 moving window. If the number of valid shadow pixels within a 5 × 5 window is less than three, a larger window (10 × 10) was adopted. This

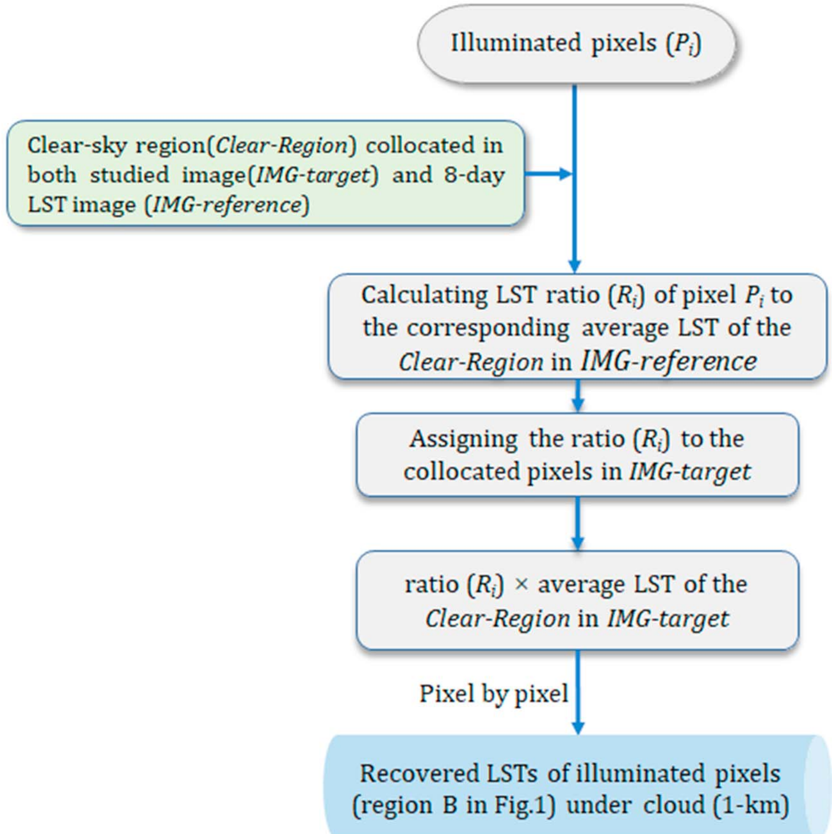

Figure 6. Flowchart to recover the LST of the illuminated pixels covered by clouds (region B in Figure 1) on the image. LST = land surface temperature.

approximation was also performed pixel by pixel until each pixel in region C was assigned a valid LST. Note that considering the fact that the temperatures of different land covers (e.g., bare soil, snow/ice, water, and vegetation) are different, the MODIS land cover product was also incorporated and only the shadow pixels with the same land covers as the studied pixel were accounted for in the moving window.

4. Results

4.1. Examination of the Landsat-8 Cloud Top Height Based on the Optimization

In section 3.2, the cloud top height was initially estimated using equation (3). Owing to the inaccuracy of the derived cloud top height, an optimization scheme was then applied to refine it. In this section, a comparison (Figure 7) was conducted to examine the performance of the optimized scheme. The green polygons shown on Figure 7 indicate the predicted cloud shadows using the optimized method. It is not difficult to see that, on the whole, the shadow areas are correctly discriminated, although some discrepancies still exist, especially in the regions of shadow boundaries. These discrepancies in position matching are mainly attributed to (1) the uncertainty in cloud detection and cloud height estimation for the cloud boundary pixels—generally, the cloudy pixels located around the boundary of a large cloud is optically thin, and thus, conducting an accurate cloud screening would be challenging—and (2) the variation of cloud opacity. On one hand, undetected thin clouds around the cloud boundary may cast shadows on the surface; on the other hand, the detected thin clouds may not cast shadows because of their small optical depths. Note that in the present method, all detected clouds were supposed to be optically opaque (i.e., would cast shadows on the surface). By contrast, the shadows discriminated based on equation (3) (red polygons in Figure 7) show a poor consistency with the real positions of the shadows. Moreover, some gaps frequently occur in the predicted shadows using equation (3) because of the larger uncertainties in the cloud top height derived based only on equation (3). The above analysis reveals that the optimization method is very effective.

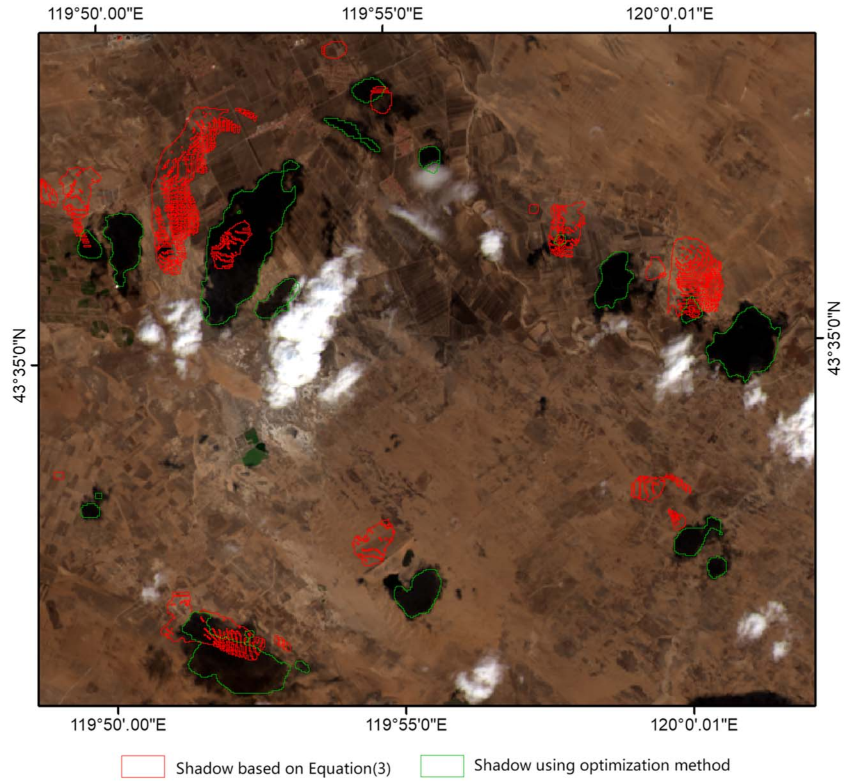

Figure 7. Predicted cloud shadows of Landsat-8 using the cloud top height derived based on equation (3) (red polygons) and the optimization scheme (green polygons).

4.2. Application to MODIS Data

In this section, MODIS-Terra images acquired at 02:55 on 22 January 2010 covering Northeast China (Figure 8), and at 04:30 (UTC) on 31 January 2010 covering part of the Tibetan plateau region (Figure 9) were randomly selected for the test. To ensure consistency, all MODIS products were reprojected to the Albers projection with WGS-84 datum, and the product with a coarse resolution was spatially resampled into a spatial resolution of 1 km using the nearest-neighbor interpolation to match the scale of the MODIS LST product. The necessary process mentioned in section 3 was performed, and the recovered MODIS cloudy sky LST is illustrated in Figures 8c and 9c. Note that a similar optimization process mentioned in section 3.2 was also applied to Figures 8 and 9 by taking all cloud pixels in the image as a big cloud.

In comparison with the MODIS false-color composite image, it can be seen that, on the whole, three cases (B, C, and D shown in Figure 1) affected by the SCSG effect can be properly characterized using the proposed scheme (Figures 8a and 9a). However, some flawed predictions are still detected in both Figures 8 and 9. The possible reasons for that can be contributed to (1) incorrect cloud detection and (2) inaccurate cloud top height for some cloud pixels even after applying an optimization process. In this paper, all cloudy pixels in an image were treated as a whole 2-D layer during the optimization. Although the optimized cloud height is reasonable for most cloud pixels, it is probably not accurate for some pixels, especially for an image covering large regions. In addition, in Figure 9, we can see the cloud on the left portion of the figure looks much bigger than that identified by the mask. That is because (1) some cloudy pixels are not correctly detected and (2) the snow cover occurs in this area; that is, not all white pixels shown in RGB image are clouds. Of course, the mixture of snow and cloud would be another contribution for this discrepancy.

It is not difficult to see that MODIS fails to provide a valid LST for a large portion of the original images due to the presence of cloud (Figures 8b and 9b). This situation has been greatly improved using the suggested scheme (Figures 8c and 9c) where the fraction of valid LSTs increases from 30% to 41% for Figure 8 and from 40% to 65% for Figure 9. However, the LST recovery is dependent on the correct identification of the three cases affected by the SCSG (i.e., regions B, C, and D in Figure 1). Therefore, uncertainties in the position

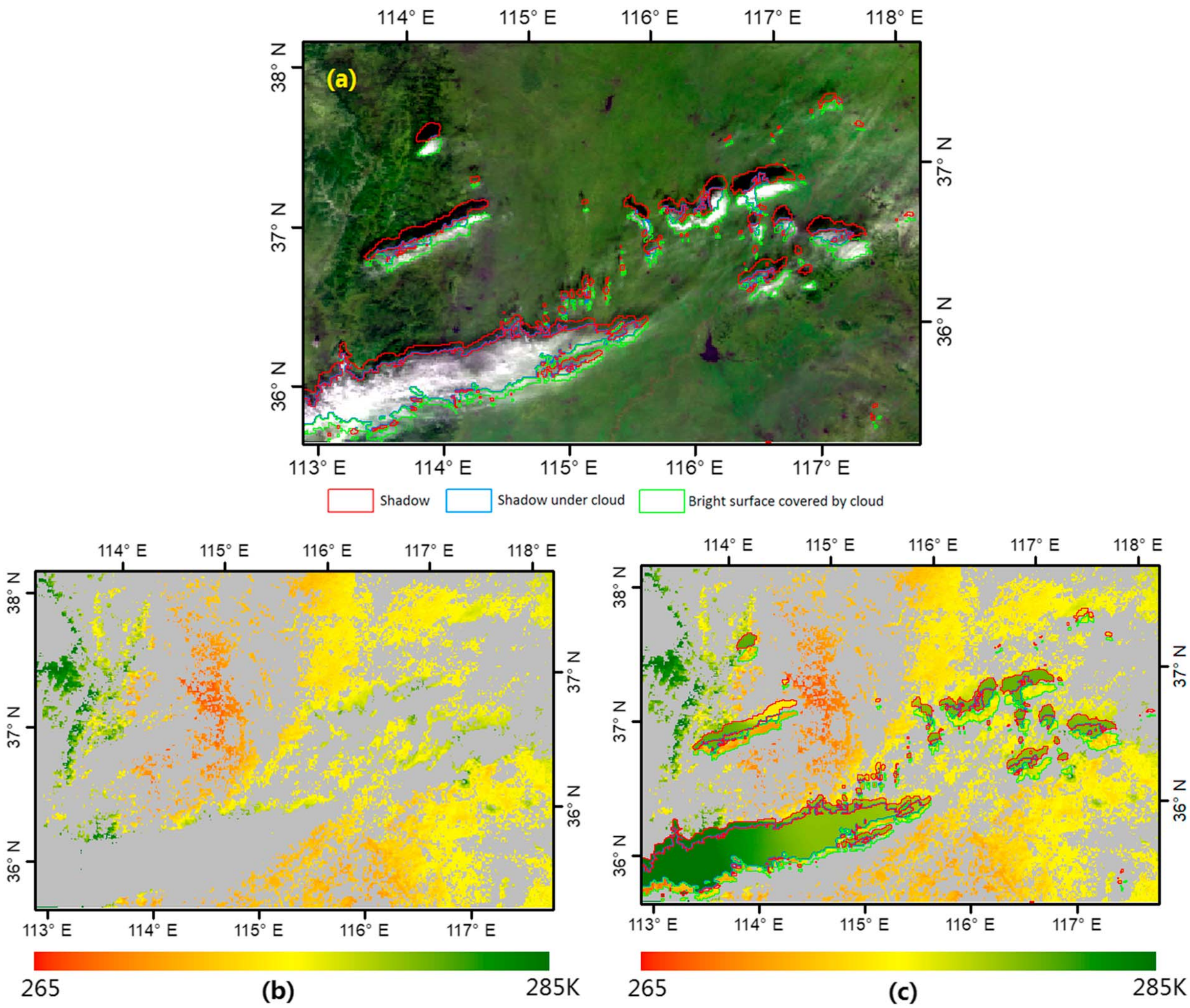

Figure 8. Recovered land surface temperature (LST) for Moderate Resolution Imaging Spectroradiometer (MODIS) data on 22 January 2010 by considering the solar-cloud-satellite geometry. (a) MODIS bands 1–3 for R, G, and B with three cases influenced by solar-cloud-satellite geometry overlapped; (b) MODIS LST product; (c) recovered MODIS LST based on the proposed scheme.

prediction could result in an unsatisfactory LST reconstruction. This issue will be highlighted in the discussion section.

4.3. Application to Landsat-8 Imagery

Similar to the above analysis based on the MODIS data, the scheme is also applied to the relatively high-resolution Landsat-8 imagery. The Landsat-8 image collected on 9 April 2015 (path, 122; row, 30) was randomly selected for this case study, and the corresponding Landsat-8 image collected on 24 March 2015 was used as a clear-sky reference map (i.e., *IMG-reference*).

Given the cloud top height and the solar and observing angles, the scopes of clouds and the corresponding shadows can be straightforwardly calculated according to equations (1) and (2). Consequently, the map of recovered LST was generated (Figure 10) based on the proposed scheme along with the reference LST map. Although some mismatches still occur, in general, the predicted scopes of regions B, C, and D in the Landsat-8 image are relatively accurate than those of the abovementioned MODIS data due to its reliable cloud height estimation. Figure 10 shows that the vast majority of LSTs in the regions of cases B and C (Figure 1) can be recovered and a spatially continuous LST image can be produced using the proposed method.

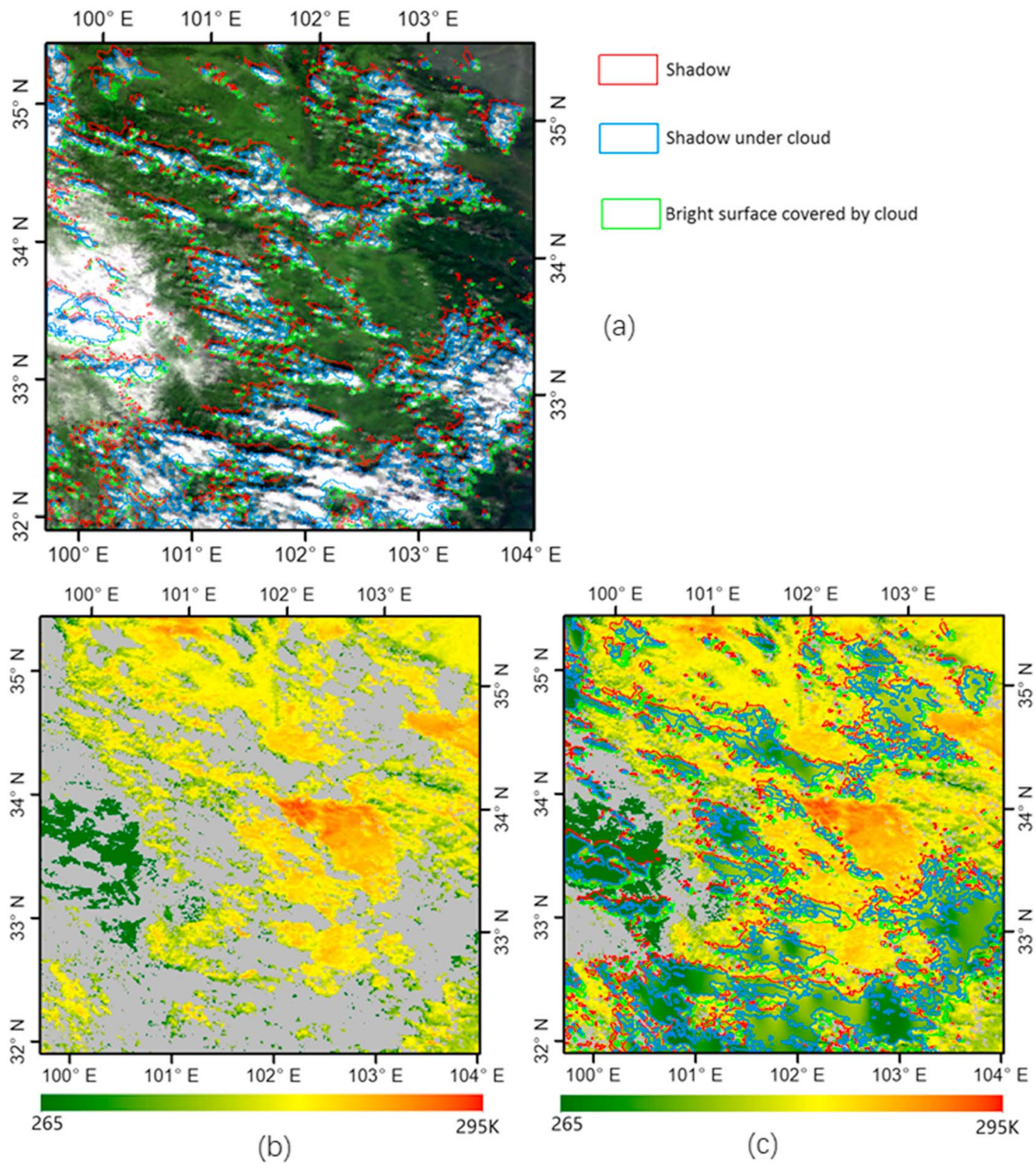

Figure 9. Recovered land surface temperature (LST) for the Moderate Resolution Imaging Spectroradiometer (MODIS) data on 31 January 2010 by considering the solar-cloud-satellite geometry. (a) MODIS bands 1–3 for R, G, and B with three cases influenced by solar-cloud-satellite geometry overlapped; (c) MODIS LST product; (d) recovered MODIS LST based on the proposed scheme.

4.4. Performance Assessment of the Proposed Scheme

In sections 4.2 and 4.3, the performance of the proposed method has been visually examined. The analysis indicates that in general, the scopes of the clouds and shadows on the image can be reasonably discriminated. The shadow pixels covered by clouds (region C in Figure 1) were assigned low LST values, and the illuminated pixels (region B in Figure 1), which are covered by the clouds in the image, were recovered with higher LST values. Theoretically, the recovered LSTs should be very close to the real state of the surface according to our scheme described in section 3. To further quantitatively examine the LST reliability of the proposed scheme, a validation against ground-based LST measurements using MODIS data was conducted.

The MODIS data used for the validation covered 5 months in the year 2016 (January, March, May, July, and September) over the United States. The Ground-based LSTs were collected from seven SURFRAD sites

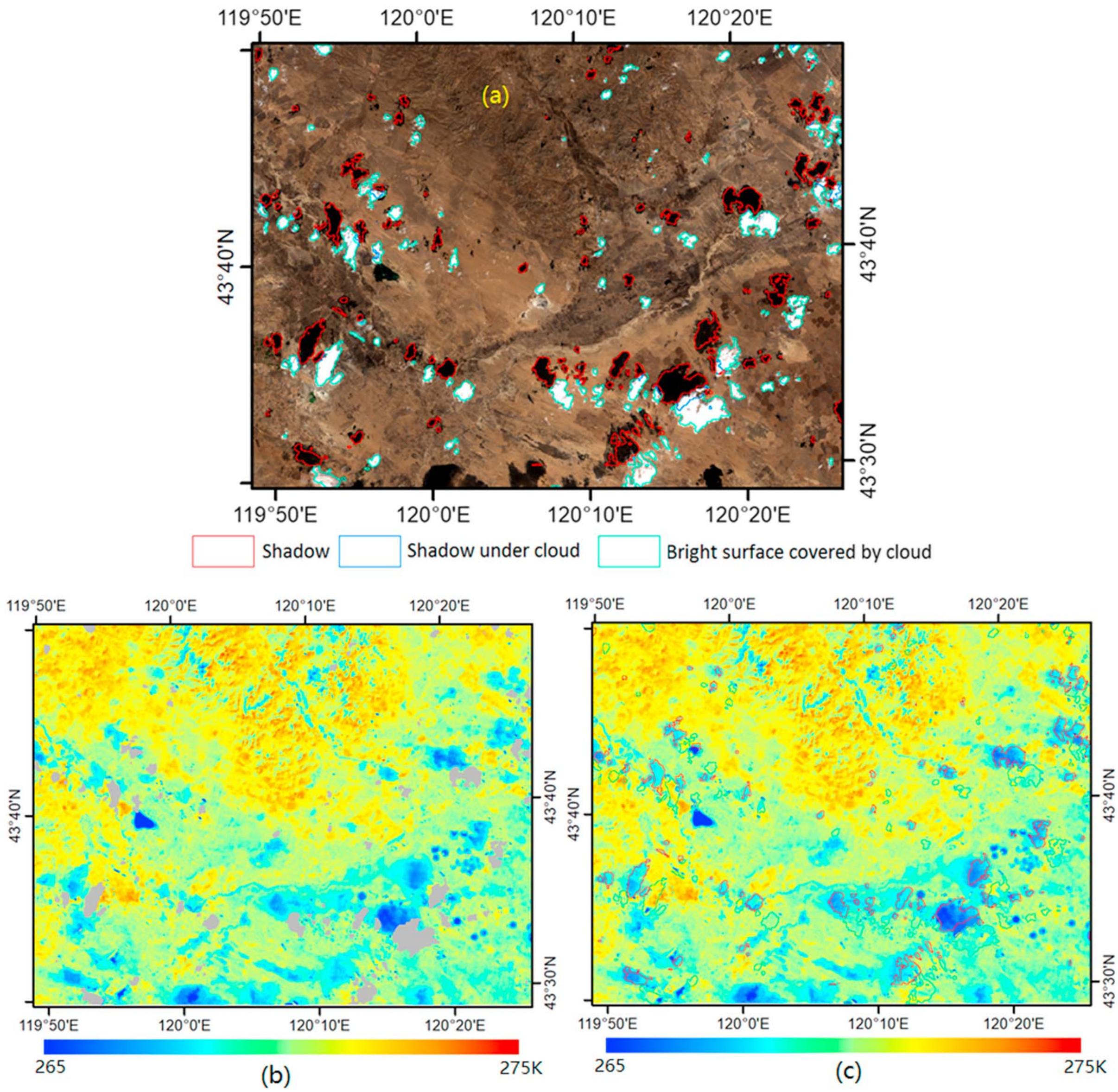

Figure 10. Recovered land surface temperature (LST) for Landsat-8 imagery by considering the solar-cloud-satellite geometry. (a) Landsat-8 bands 4, 3, and 2 for R, G, and B with three cases influenced by solar-cloud-satellite geometry overlapped; (b) Landsat-8 LST under clear-sky conditions, with the gray pixels indicating clouds; (c) recovered LST based on the proposed scheme.

(Bondville, Boulder, Desert Rock, Fort Peck, Goodwin Creek, Sioux Falls and Penn. State Univ.; Augustine et al., 2000). The data are available at http://www.srrb.noaa.gov/surfrad/ and are collected with a 1-min average. Note that the SURFRAD sites do not directly measure the LSTs but only provide related upward and downward longwave radiation. To deduce the LST from the longwave radiation, equation (5) was used here to convert the longwave radiation to the corresponding LST.

$$LST = \left(\frac{LWUR - LWDR \times (1-\varepsilon)}{\sigma\varepsilon}\right)^{1/4}, \tag{5}$$

where LWUR and LWDR are the surface longwave upward and downward radiation, respectively, which are directly measured at the sites; ε is the broadband surface emissivity at the site, which was estimated according to the work of Cheng et al. (2013), which utilized both the MOD11_L2 and MOD11B1 products; and σ is the Stefan-Boltzmann constant (5.6703×10^{-8} W·m^{-2}·K^{-4}).

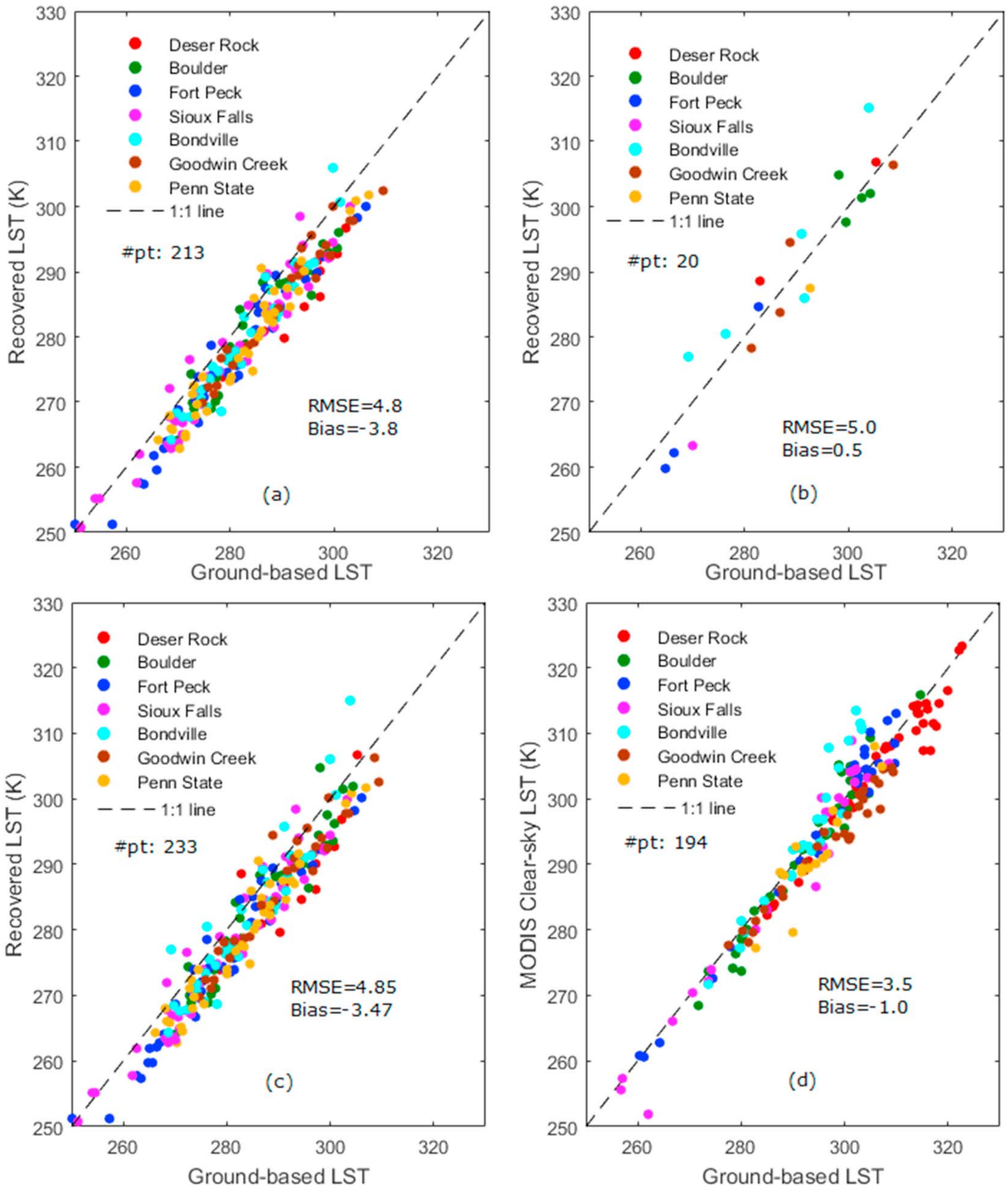

Figure 11. Validation of the proposed scheme versus the ground measurements at the seven Surface Radiation Budget Network (SURFRAD) sites. (a) Shadow pixels covered by clouds (region C in Figure 1); (b) bright surface covered by clouds (region B in Figure 1); (c) data of all cases (a + b); and (d) MODIS LST under clear-sky conditions. LST = land surface temperature; MODIS = Moderate Resolution Imaging Spectroradiometer; RMSE = root mean square error.

For each site, the ground-based LST measurements (converted using equation (5)) closest to the time of the MODIS overpass were used as reference to compare with the recovered LSTs. No special consideration was given for spatial match, that is, the LST of the pixel wherein the site located was directly used for comparison with the ground measurements. During the assessment, only data pairs influenced by the SCSG effect (i.e., cases B and C in Figure 1) but were invalid in the MODIS LST product were retained and compared. In total, 233 points were collected and the comparison between the recovered and the ground-based LSTs is shown in Figure 11. To better examine the reliability of the recovered LST, the MODIS clear-sky LSTs collected in the same time period versus the ground-based measurements were also compared (Figure 11d). The scatterplot reveals that in general, the recovered LSTs show a reasonable agreement with the ground measurements with root mean square error (RMSE) < 4.9 K and bias < 3.5 K. In comparing with the clear-sky validation

(Figure 11d), the RMSE of the recovered LST is slightly larger (4.9 vs. 3.5 K), while the bias is clearly cold biased (−3.47 vs. −1.0 K). The relatively large low-bias (−3.47 K) mainly results from the contribution of the shadow pixels under the clouds (region C in Figure 1), as shown in Figure 11a. In accordance with the above analysis, the cold bias can be explained by (1) the undetected cloud in the MODIS LST product —some thin clouds are probably treated as valid clear-sky shadow pixels. This can be evidenced by a cold bias in the clear-sky LSTs shown in Figure 11d in which a bias of −1 .0 K was also detected—and (2) the large window used in searching for nearby shadow pixels. Although they are all shadow pixels, the LSTs may have some difference, especially for the pixels that are relatively far away from the one being studied. This issue is highlighted in the following discussion section. In contrast, almost no bias was detected for the bright pixels covered by clouds (region B in Figure 1). It should be noted that only 20 points were collected here (Figure 11b). In addition, no site dependence was found for each of the four cases in Figure 11 for both RMSE and bias.

Although the performance of the proposed scheme is not accurate enough compared with the clear-sky LST retrievals as shown in Figure 11d, the proposed scheme provides an important idea for studying surface energy and water cycles based on LST, especially under cloudy sky conditions. To some extent, this study proves the feasibility of the proposed scheme.

Note that an alternative way to perform validation is to directly compare the derived longwave flux with the ground-based longwave flux, considering that the SURFRAD can only provide flux measurements. However, the derived longwave radiation based on the recovered LST is the surface emitted radiation, not the surface upward radiation (emitted radiation plus the reflected longwave downward radiation), which is provided by the SURFRAD sites. In this case, the site measurements have to be converted to the surface emitted radiation, in which the broadband emissivity is still an indispensable input variable. Therefore, in this study, the LSTs were extracted at those SURFRAD sites and then compared with the derived LSTs.

4.5. Error Analysis and Discussion

For the proposed scheme to reconstruct LST under cloudy sky conditions, the key steps include (1) determination of specific positions and scopes of clouds and shadows and (2) approximation of the LSTs of the cloud-covered pixels in the image based on the LSTs that are spatially and temporally close to the pixels recovered. The possible error sources associated with the new scheme can be grouped into four points: (1) uncertainty in cloud top height, which is considered to be the largest source of uncertainty of the new scheme (see analyses in sections 4.1–4.3)—as discussed in section 4.2, the cloud top height is an essential variable to calculate the projected position of clouds and shadows. Any uncertainty in cloud height can definitely lead to inaccurate identification of the three cases affected by the SCSG, which in turn affect the accuracy of LST reconstruction—(2) misjudgment in cloud detection—theoretically, based on the proposed method, all LSTs of the cloud-contaminated pixels can be recovered. However, cloud or shadow misjudgment frequently occurs in many cases (see Figure 3), thus resulting in inaccurate LST approximations—(3) reliability of the clear-sky LST estimations—in our case, the MODIS 8-day LST or the temporally closest Landsat-8 image was chosen to serve as the reference LST image. The data quality of the reference images and/or the variations in land covers (e.g., snow/ice, water, and vegetation surfaces during growing season) may affect the accuracy of the recovered LST. Specifically, the unidentified cloud or the mixing between cloud and snow/ice is a possible source of error in the clear-sky LST for both the target and the reference image—and (4) the LST representativeness of the nearby shadow pixels. The LSTs of the shadow pixels under a cloud were approximated using those of the nearby shadow pixels by assuming that the nearby shadow pixels have similar temperatures to the target pixel. Although our statistics reveals that the LST variation for all cloudy pixels within a MODIS image is relatively small, the difference indeed exists for certain land covers or certain seasons. Furthermore, the cloud boundary pixels, especially the thin cloud, may be deemed as valid in the LST product. This is a possible cause of the cold bias in the validation. In addition, the window size used to search the nearby shadow pixels, as described in section 3.3.2, is also a source of error for the cold bias. Of course, under overcast skies, although the method used to determine the scopes of regions B, C, and D (Figure 1) can still work, most predicted areas are corresponding to shadow pixels under clouds (region C in Figure 1); thus, it is hard to recover the LST in region C under overcast conditions if we do not know the LST of the valid shadow pixels (region D), which should be visible to the sensor.

In addition to the abovementioned factors, we must admit that there are still some uncertainties in the present version of the proposed scheme (such as the homogenous treatment of the cloud layer, the assumption of similar LST ratio in target and reference images), so a lot of work is required in the future to provide a reliable LST data set that meets the accuracy requirement of modeling/monitoring applications. One point that needs to be addressed is that although it is very important, for a long time, the estimation of LST under cloudy sky conditions has been a great challenge to the Earth-observing community. In this study, we have taken a step forward in estimating cloudy sky LST based on the SCSG, and the findings of this study demonstrate the proof of concept of an LST-recovery scheme, which could significantly increase the coverage of remotely sensed LST products.

5. Conclusions

As is known to the Earth observation science community, clouds have a strong effect on remotely sensed LST by almost completely absorbing the surface emitted thermal energy. Most LST products derived from various algorithms are spatially discontinuous due to cloud contamination. However, we can take advantage of the SCSG effect to recover the LST of cloudy pixels to some extent. To this end, a scheme to recover the LST under the cloud is proposed by taking MODIS and Landsat-8 images as test data.

The new scheme approximates the LST under cloudy skies by classifying the image into four cases, namely, clear-sky pixels, cloud shadow pixels (region D), shadow under a cloud (region C), and bright surface covered by a cloud (region B) (see Figure 1) by considering the cloud top height, the solar, and observing angles. Then, the LSTs of regions B and C were separately recovered by using the reference LST under clear-sky days, which are temporally close to the image being recovered or estimated using the nearby shadow pixels. Although not as accurate as those under clear-sky conditions, the validation results indicate that the recovered LSTs show reasonable agreement with the ground-based LSTs measurements with bias < 3.5 K and RMSE < 4.9 K. The application of the new method to MODIS and Landsat-8 data reveals that the LSTs of cloudy pixels can be recovered and that the fraction of valid LSTs in an image can be correspondingly improved.

It should be noted that although the MODIS and Landsat-8 data were used in this study, the new method is not data specific. Instead, it can be used in other remote-sensing data (such as Visible Infrared Imaging Radiometer Suite (VIIRS) and Advanced Very High Resolution Radiometer (AVHRR)) as long as the required input variables, such as solar and observing angles, cloud top height and reference LST maps are provided. Although it still has rooms for improvement, the new scheme provides an alternative manner to derive cloudy sky LST based only on optical remote sensing data. Meanwhile, it also gives some inspiration to the remote sensing community, especially in the field of surface energy balance.

Acknowledgments
The work in this paper is supported by the National Natural Science Foundation of China (NSFC) project (41571364), National key basic research program of China (2015CB953701), and NSFC project (41771387). The MODIS products used in this work are downloaded from https://search.earthdata.nasa.gov/. The landsat-8 data are collected from the Earthdata Search – NASA website (https://earthexplorer.usgs.gov/). The SURFRAD data are available at the Earth System Research Laboratory website (http://www.srrb.noaa.gov/surfrad/). All other data used are listed in the references. We are grateful to the four anonymous reviewers for their valuable comments on our study with which the quality of our paper has been greatly improved.

References

Augustine, J. A., DeLuisi, J. J., & Long, C. N. (2000). SURFRAD—A national surface radiation budget network for atmospheric research. *Bulletin of the American Meteorological Society*, *81*(10), 2341–2357. https://doi.org/10.1175/1520-0477(2000)081<2341:SANSRB>2.3.CO;2

Baehr, J., Fröhlich, K., Botzet, M., Domeisen, D. I. V., Kornblueh, L., Notz, D., et al. (2015). The prediction of surface temperature in the new seasonal prediction system based on the MPI-ESM coupled climate model. *Climate Dynamics*, *44*(9–10), 2723–2735. https://doi.org/10.1007/s00382-014-2399-7

Becker, F., & Li, Z.-L. (1990). Towards a local split window method over land surfaces. *International Journal of Remote Sensing*, *11*(3), 369–393. https://doi.org/10.1080/01431169008955028

Brunsell, N. A., & Gillies, R. R. (2003). Length scale analysis of surface energy fluxes derived from remote sensing. *Journal of Hydrometeorology*, *4*(6), 1212–1219. https://doi.org/10.1175/1525-7541(2003)004<1212:LSAOSE>2.0.CO;2

Chen, X., Long, D., Hong, Y., Zeng, C., & Yan, D. (2017). Improved modeling of snow and glacier melting by a progressive two-stage calibration strategy with GRACE and multisource data: How snow and glacier meltwater contributes to the runoff of the Upper Brahmaputra River basin? *Water Resources Research*, *53*, 2431–2466. https://doi.org/10.1002/2016WR019656

Cheng, J., Liang, S., Yao, Y., & Zhang, X. (2013). Estimating the optimal broadband emissivity spectral range for calculating surface longwave net radiation. *IEEE Geoscience and Remote Sensing Letters*, *10*(2), 401–405. https://doi.org/10.1109/LGRS.2012.2206367

Cosgrove, B. A., Lohmann, D., Mitchell, K. E., Houser, P. R., Wood, E. F., Schaake, J. C., et al. (2003). Real-time and retrospective forcing in the North American Land Data Assimilation System (NLDAS) project. *Journal of Geophysical Research*, *108*(D22), 8842. https://doi.org/10.1029/2002JD003118

Du, C., Ren, H., Qin, Q., Meng, J., & Zhao, S. (2015). A practical split-window algorithm for estimating land surface temperature from Landsat 8 data. *Remote Sensing*, *7*(1), 647–665. https://doi.org/10.3390/rs70100647

Duan, S. B., Li, Z. L., & Leng, P. (2017). A framework for the retrieval of all-weather land surface temperature at a high spatial resolution from polar-orbiting thermal infrared and passive microwave data. *Remote Sensing of Environment*, *195*, 107–117. https://doi.org/10.1016/j.rse.2017.04.008

Eckardt, R., Berger, C., Thiel, C., & Schmullius, C. (2013). Removal of optically thick clouds from multi-spectral satellite images using multi-frequency SAR data. *Remote Sensing*, *5*(6), 2973–3006. https://doi.org/10.3390/rs5062973

Giglio, L., Descloitres, J., Justice, C. O., & Kaufman, Y. J. (2003). An enhanced contextual fire detection algorithm for MODIS. *Remote Sensing of Environment*, *87*(2-3), 273–282. https://doi.org/10.1016/S0034-4257(03)00184-6

Gillespie, A. R., Rokugawa, S., Matsunaga, T., Cothern, J. S., Hook, S., & Kahle, A. B. (1998). A temperature and emissivity separation algorithm for Advanced Spaceborne Thermal Emission and Reflection Radiometer (ASTER) images. *IEEE Transactions on Geoscience and Remote Sensing*, *36*(4), 1113–1126. https://doi.org/10.1109/36.700995

Hagolle, O., Huc, M., Pascual, D. V., & Dedieu, G. (2010). A multi-temporal method for cloud detection, applied to Formosat-2, Venmus, Landsat and Sentinel-2 images. *Remote Sensing of Environment*, *114*(8), 1747–1755. https://doi.org/10.1016/j.rse.2010.03.002

Hu, G., & Jia, L. (2015). Monitoring of evapotranspiration in a semi-arid inland river basin by combining microwave and optical remote sensing observations. *Remote Sensing*, *7*(3), 3056–3087. https://doi.org/10.3390/rs70303056

Hulley, G. C., & Hook, S. J. (2011). Generating consistent land surface temperature and emissivity products between ASTER and MODIS data for earth science research. *IEEE Transactions on Geoscience and Remote Sensing*, *49*(4), 1304–1315. https://doi.org/10.1109/TGRS.2010.2063034

Jiao, Z., Yan, G., Zhao, J., Wang, T., & Chen, L. (2015). Estimation of surface upward longwave radiation from MODIS and VIIRS clear-sky data in the Tibetan Plateau. *Remote Sensing of Environment*, *162*, 221–237. https://doi.org/10.1016/j.rse.2015.02.021

Jiménez-Munoz, J. C., Cristobal, J., Sobrino, J. A., Soria, G., Ninyerola, M., & Pons, X. (2009). Revision of the single-channel algorithm for land surface temperature retrieval from Landsat thermal-infrared data. *IEEE Transactions on Geoscience and Remote Sensing*, *47*, 339–349.

Jiménez-Muñoz, J. C., & Sobrino, J. A. (2003). A generalized single-channel method for retrieving land surface temperature from remote sensing data. *Journal of Geophysical Research*, *108*(D22), 4688. https://doi.org/10.1029/2003JD003480

Jiménez-Muñoz, J. C., Sobrino, J. A., Skoković, D., Mattar, C., & Cristóbal, J. (2014). Land surface temperature retrieval methods from Landsat-8 thermal infrared sensor data. *IEEE Geoscience and Remote Sensing Letters*, *11*(10), 1840–1843. https://doi.org/10.1109/LGRS.2014.2312032

Julien, Y., & Sobrino, J. A. (2009). The Yearly Land Cover Dynamics (YLCD) method: An analysis of global vegetation from NDVI and LST parameters. *Remote Sensing of Environment*, *113*(2), 329–334. https://doi.org/10.1016/j.rse.2008.09.016

Justice, C. O., Townshend, J. R. G., Vermote, E. F., Masuoka, E., Wolfe, R. E., Saleous, N., et al. (2002). An overview of MODIS land data processing and product status. *Remote Sensing of Environment*, *83*(1-2), 3–15. https://doi.org/10.1016/S0034-4257(02)00084-6

Kalma, J. D., McVicar, T. R., & McCabe, M. F. (2008). Estimating land surface evaporation: A review of methods using remotely sensed surface temperature data. *Surveys in Geophysics*, *29*(4-5), 421–469. https://doi.org/10.1007/s10712-008-9037-z

Kustas, W., & Anderson, M. (2009). Advances in thermal infrared remote sensing for land surface modeling. *Agricultural and Forest Meteorology*, *149*(12), 2071–2081. https://doi.org/10.1016/j.agrformet.2009.05.016

Li, J., Liu, C., Huang, H., Schmit, T. J., Wu, X., Menzel, W., & Gurka, J. J. (2005). Optimal cloud-clearing for AIRS radiances using MODIS. *IEEE Transactions on Geoscience and Remote Sensing*, *43*, 1266–1278.

Li, Z. L., Tang, B. H., Wu, H., Ren, H., Yan, G., Wan, Z., et al. (2013). Satellite-derived land surface temperature: Current status and perspectives. *Remote Sensing of Environment*, *131*, 14–37. https://doi.org/10.1016/j.rse.2012.12.008

Lv, H., Wang, Y., & Shen, Y. (2016). An empirical and radiative transfer model based algorithm to remove thin clouds in visible bands. *Remote Sensing of Environment*, *179*, 183–195. https://doi.org/10.1016/j.rse.2016.03.034

Lyapustin, A., Wang, Y., & Frey, R. (2008). An automatic cloud mask algorithm based on time series of MODIS measurements. *Journal of Geophysical Research*, *113*, D16207. https://doi.org/10.1029/2007JD009641

Ma, X. L., Wan, Z., Moeller, C. C., Menzel, W. P., & Gumley, L. E. (2002). Simultaneous retrieval of atmospheric profiles, land-surface temperature, and surface emissivity from Moderate-Resolution Imaging Spectroradiometer thermal infrared data: Extension of a two-step physical algorithm. *Applied Optics*, *41*(5), 909–924. https://doi.org/10.1364/AO.41.000909

Ma, X. L., Wan, Z., Moeller, C. C., Menzel, W. P., Gumley, L. E., & Zhang, Y. (2000). Retrieval of geophysical parameters from Moderate Resolution Imaging Spectroradiometer thermal infrared data: Evaluation of a two-step physical algorithm. *Applied Optics*, *39*(20), 3537–3550. https://doi.org/10.1364/AO.39.003537

Ma, Y., Kuang, Y., & Huang, N. (2010). Coupling urbanization analyses for studying urban thermal environment and its interplay with biophysical parameters based on TM/ETM+ imagery. *International Journal of Applied Earth Observation and Geoinformation*, *12*(2), 110–118. https://doi.org/10.1016/j.jag.2009.12.002

Mao, K., Qin, Z., Shi, J., & Gong, P. (2005). A practical split-window algorithm for retrieving land-surface temperature from MODIS data. *International Journal of Remote Sensing*, *26*(15), 3181–3204. https://doi.org/10.1080/01431160500044713

Mao, K., Shi, J., Tang, H., Li, Z. L., Wang, X., & Chen, K. S. (2008). A neural network technique for separating land surface emissivity and temperature from ASTER imagery. *IEEE Transactions on Geoscience and Remote Sensing*, *46*(1), 200–208. https://doi.org/10.1109/TGRS.2007.907333

Masuoka, E., Fleig, A., Wolfe, R. E., & Patt, F. (1998). Key characteristics of MODIS data products. *IEEE Transactions on Geoscience and Remote Sensing*, *36*(4), 1313–1323. https://doi.org/10.1109/36.701081

Mercury, M., Green, R., Hook, S., Oaida, B., Wu, W., Gunderson, A., & Chodas, M. (2012). Global cloud cover for assessment of optical satellite observation opportunities: A HyspIRI case study. *Remote Sensing of Environment*, *126*, 62–71. https://doi.org/10.1016/j.rse.2012.08.007

Paudel, K. P., & Andersen, P. (2011). Monitoring snow cover variability in an agropastoral area in the trans Himalayan region of Nepal using MODIS data with improved cloud removal methodology. *Remote Sensing of Environment*, *115*(5), 1234–1246. https://doi.org/10.1016/j.rse.2011.01.006

Paul, M., Aires, F., Prigent, C., Trigo, I. F., & Bernardo, F. (2012). An innovative physical scheme to retrieve simultaneously surface temperature and emissivities using high spectral infrared observations from IASI. *Journal of Geophysical Research*, *117*, D11302. https://doi.org/10.1029/2011JD017296

Pielke, R. A., Avissar, R., Raupach, M., Dolman, A. J., Zeng, X., & Denning, A. S. (1998). Interactions between the atmosphere and terrestrial ecosystems: Influence on weather and climate. *Global Change Biology*, *4*(5), 461–475. https://doi.org/10.1046/j.1365-2486.1998.t01-1-00176.x

Qian, Y. G., Zhao, E. Y., Gao, C., Wang, N., & Ma, L. (2015). Land surface temperature retrieval using nighttime mid-infrared channels data from Airborne Hyperspectral Scanner. *IEEE Journal of Selected Topics in Applied Earth Observations and Remote Sensing*, *8*(3), 1208–1216.

Qin, Z., Karnieli, A., & Berliner, P. (2001). A mono-window algorithm for retrieving land surface temperature from Landsat TM data and its application to the Israel-Egypt border region. *International Journal of Remote Sensing*, *22*(18), 3719–3746. https://doi.org/10.1080/01431160010006971

Ren, H., Du, C., Liu, R., Qin, Q., Yan, G., Li, Z. L., & Meng, J. (2015). Atmospheric water vapor retrieval from Landsat 8 thermal infrared images. *Journal of Geophysical Research: Atmospheres*, *120*, 1723–1738. https://doi.org/10.1002/2014JD022619

Sobrino, J. A., Jiménez-Munoz, J. C., El-Kharraz, J., Gómez, M., Romaguera, M., & Sòria, G. (2004). Single-channel and two-channel methods for land surface temperature retrieval from DAIS data and its application to the Barrax site. *International Journal of Remote Sensing*, *25*(1), 215–230. https://doi.org/10.1080/0143116031000115210

Sobrino, J. A., Jiménez-Muñoz, J. C., & Paolini, L. (2004). Land surface temperature retrieval from LANDSAT TM 5. *Remote Sensing of Environment*, *90*(4), 434–440. https://doi.org/10.1016/j.rse.2004.02.003

Sobrino, J. A., Li, Z.-L., Stoll, M. P., & Becker, F. (1994). Improvements in the split-window technique for land surface temperature determination. *IEEE Transaction on Geosciences and Remote Sensing*, *32*(2), 243–253. https://doi.org/10.1109/36.295038

Sobrino, J. A., Li, Z.-L., Stoll, M. P., & Becker, F. (1996). Multi-channel and multi-angle algorithms for estimating sea and land surface temperature with ATSR data. *International Journal of Remote Sensing*, *17*(11), 2089–2114. https://doi.org/10.1080/01431169608948760

Tang, B.-H., Bi, Y., Li, Z.-L., & Xia, J. (2008). Generalized Split-Window algorithm for estimate of land surface temperature from Chinese geostationary FengYun meteorological satellite (FY-2C) data. *Sensors*, *8*(2), 933–951. https://doi.org/10.3390/s8020933

Tang, R., Li, Z. L., Sun, X., & Bi, Y. (2017). Temporal upscaling of instantaneous evapotranspiration on clear-sky days using the constant reference evaporative fraction method with fixed or variable surface resistances at two cropland sites. *Journal of Geophysical Research: Atmospheres*, *122*, 784–801. https://doi.org/10.1002/2016JD025975

Wan, Z., & Dozier, J. (1996). A generalized split-window algorithm for retrieving land-surface temperature from space. *IEEE Transactions on Geoscience and Remote Sensing*, *34*. https://doi.org/10.1109/36.508406

Wan, Z., & Li, Z.-L. (1997). A physics-based algorithm for retrieving land-surface emissivity and temperature from EOS/MODIS data. *IEEE Transactions on Geoscience and Remote Sensing*, *35*, 980–996.

Wan, Z., Wang, P., & Li, X. (2004). Using MODIS land surface temperature and normalized difference vegetation index products for monitoring drought in the southern Great Plains, USA. *International Journal of Remote Sensing*, *25*(1), 61–72. https://doi.org/10.1080/0143116031000115328

Wang, T., Shi, J., Husi, L., Zhao, T., Ji, D., Xiong, C., & Gao, B. (2017). Effect of solar-cloud-satellite geometry on land surface shortwave radiation derived from remotely sensed data. *Remote Sensing*, *9*(7), 690. https://doi.org/10.3390/rs9070690

Wang, T., Yan, G., & Chen, L. (2012). Consistent retrieval methods to estimate land surface shortwave and longwave radiative flux components under clear-sky conditions. *Remote Sensing of Environment*, *124*, 61–71. https://doi.org/10.1016/j.rse.2012.04.026

Wang, W., Liang, S., & Augustine, J. A. (2009). Estimating high spatial resolution clear-sky land surface upwelling longwave radiation from MODIS data. *IEEE Transactions on Geoscience and Remote Sensing*, *47*(5), 1559–1570. https://doi.org/10.1109/TGRS.2008.2005206

Weng, Q. (2009). Thermal infrared remote sensing for urban climate and environmental studies: Methods, applications, and trends. *ISPRS Journal of Photogrammetry and Remote Sensing*, *64*(4), 335–344. https://doi.org/10.1016/j.isprsjprs.2009.03.007

Xue, B. L., Wang, L., Yang, K., Tian, L., Qin, J., Chen, Y., et al. (2013). Modeling the land surface water and energy cycles of a mesoscale watershed in the central Tibetan Plateau during summer with a distributed hydrological model. *Journal of Geophysical Research: Atmospheres*, *118*, 8857–8868. https://doi.org/10.1002/jgrd.50696

Yan, G., Wang, T., Jiao, Z., Mu, X., Zhao, J., & Chen, L. (2016). Topographic radiation modeling and spatial scaling of clear-sky land surface longwave radiation over rugged terrain. *Remote Sensing of Environment*, *172*, 15–27. https://doi.org/10.1016/j.rse.2015.10.026

Zhu, Z., & Woodcock, C. E. (2014). Automated cloud, cloud shadow, and snow detection in multitemporal Landsat data: An algorithm designed specifically for monitoring land cover change. *Remote Sensing of Environment*, *152*, 217–234. https://doi.org/10.1016/j.rse.2014.06.012